sustainability

MDPI

*Article*

# Comparative Evaluation of the Immersed-Solid Method for Simulating the Flow Field around Hydrofoil

**Zilong Hu [1], Di Zhu [2,*], Ruofu Xiao [1,3] and Ran Tao [1,3]**

[1] College of Water Resources and Civil Engineering, China Agricultural University, Beijing 100083, China
[2] College of Engineering, China Agricultural University, Beijing 100083, China
[3] Beijing Engineering Research Center of Safety and Energy Saving Technology for Water Supply Network System, China Agricultural University, Beijing 100083, China
* Correspondence: zhu_di@cau.edu.cn

**Abstract:** The wall boundary is important in computational-fluid-dynamics simulations. If extremely small leakage, changing leakage or a moving body exists in the simulation case, the difficulty in meshing and solving near-wall flow increases. The immersed-solid method, which inserts a rigid, solid body into the entire fluid domain, was a choice to solve the wall-boundary-solution problems mentioned above, without considering mesh deformation. The purpose of this paper is to verify the effectiveness of the immersed-solid method in the simulation of extremely small leakage, changing leakage or a moving body, and to provide a theoretical basis for the use of the submerged-solid method in engineering. In this study, the NACA0015 hydrofoil was used to check the hydrodynamic characteristics in using the immersed-solid method. The comparative study was conducted at the incidence angle of 8 degrees and a Reynolds number of $5.0 \times 10^5$, by using the immersed-solid and traditional no-slip-wall boundary. The results show that the flow striking and separation with pressure rise and drop can be correctly captured using an immersed-solid setup with boundary tracking. However, the accuracy of pressure and velocity field using the immersed-solid method was insufficient. The turbulence-kinetic energy was much higher around the immersed-solid foil body. Generally, the immersed-solid method can qualitatively predict the correct hydrodynamic characteristics. Its convergence ability is better, and it can save approximately 20% of CPU time, even if the grid density is 4.39 times of the traditional no-slip wall. Therefore, the immersed-solid method can be a good choice for engineering-flow cases with complex wall problems.

**Keywords:** wall boundary; immersed-solid method; turbulent flow; hydrofoil

check for updates

**Citation:** Hu, Z.; Zhu, D.; Xiao, R.; Tao, R. Comparative Evaluation of the Immersed-Solid Method for Simulating the Flow Field around Hydrofoil. *Sustainability* **2023**, *15*, 3493. https://doi.org/10.3390/su15043493

Academic Editors: Bin Huang, Ling Zhou, Yuquan Zhang and Jianhua Zhang

Received: 9 January 2023
Revised: 10 February 2023
Accepted: 13 February 2023
Published: 14 February 2023

## 1. Introduction

Computational fluid dynamics (CFD) is widely used in the performance evaluation [1] and optimization [2] of hydraulic machinery. The wall boundary is the most common boundary type in computational-fluid-dynamics (CFD) simulations, especially considering fluid flows around solid bodies [3,4]. Currently, an accurate solution of near-wall flow is no more difficult. The direct solving of the usage of different wall-function estimations and mixed formulations can be applicable to wall function insensitive to y+ [5], pipe flow [6] and high Reynolds-number flow [7]. However, some near-wall puzzles still exist to be solved in modern-engineering CFD simulations. For example, extremely small leakage is difficult to simulate when it is much smaller than the other regions [8]. Putting mesh topology inside extremely small leakage is a challenge, especially without compromising the accuracy with the simulation cost. Another example is variable leakage, such as leakage in piston-pump housing and gate housing. Blanco et al. [9] used dynamic-grid technology to simulate the flow of a piston pump, and Akoz et al. [10] compared eight different grid systems to obtain a grid that can accurately simulate the flow of a sluice gate. In this case, researchers need to change both the grid-topology distribution and the density. This will strongly affect the time cost of CFD's pre-process and the solution process. Moving a solid body in fluid is also a difficult problem [11]. If the solid body only translates, the mesh-re-building process can be simplified and well solved. If translation and rotation happen together [12,13], the mesh re-building becomes difficult, and even be unable to be made automatic. The immersed-solid method has become another wall-boundary choice in the commercial software ANSYS CFX, putting a solid domain into the entire fluid domain [14]. It provides a new way for the near-wall flow simulations to solve the puzzles above. Yoon et al. [15] simplified the calculation of small-clearance leakage flow in an external gear pump by the immersed-solid method, overcoming numerical difficulties and saving calculation time. The simulation results show that there is little difference between the numerical predictions and the experimental data. Zhang et al. [16,17] applied the immersed-solid method to the simulation of moving-boundary problems which were difficult to solve by other methods, and simulated the flow field inside the double-helical pump. At present, the immersed-solid method has been widely used in the simulation of extremely small leakage, changing leakage, and the moving body, but the gap between its accuracy and the traditional wall-boundary simulation is not clear, and a good mesh-matching scheme on the fluid–solid interface has not been found.

Hydrofoil, which is a typical, simplified solid body, is chosen as the studied object in this case, due to its standardized profile. It has been widely investigated in both numerical simulations and experiments [18–21]. For typical hydrofoils, the lift/drag forces, flow-striking and separation point, surface-pressure distribution, cavitation performance and structural-response characteristics are already clear. Therefore, the hydrodynamic characteristics can be well studied for comparing the immersed-solid method with the traditional wall-boundary type [22]. In this study, there are three main points to be solved. Firstly, it is necessary to find a way to mesh the fluid domain, solid domain and the fluid–solid interface when using the immersed-solid method. The mesh independency in using the immersed-solid method and using the traditional wall boundary are checked and compared. Secondly, the flow field should be examined in detail, including the pressure field, velocity field and turbulence field. This will be helpful for the application of the immersed-solid method in engineering flow cases. Thirdly, the convergence ability should be comparatively studied in the immersed-solid case and in the traditional wall-boundary case. The time cost, hardware cost and CFD pre-processing cost need a comprehensive comparison to provide guidance for engineering cases.

## 2. Numerical Methods

### *2.1. Turbulence Modeling*

The numerical study adopts the Reynolds-averaged Navier–Stokes (RANS) equation. The RANS equation is the equation of average turbulent motion obtained by averaging the physical quantity of turbulence with the sum of an average value and a pulsation value. The eddy-viscosity turbulence model is used to close the averaged equations. It follows the Boussinesq eddy-viscosity hypothesis [23], which establishes the relationship between the eddy viscosity, $\mu_t$, and the Reynolds stress, $\tau_{ij}$. In this study, the SST turbulence model [24–26], which deals well with the strong freestream and improves the accuracy of adverse pressure gradients by combining the standard $k$-$\varepsilon$ model and Wilcox's $k$-$\omega$ model, was used. The SST model was based on the turbulence-kinetic-energy, $k$, equation and the specific-dissipation-rate, $\omega$, equation [27]:

$$\frac{\partial(\rho k)}{\partial t} + \frac{\partial(\rho u_j k)}{\partial x_j} = P_k - \beta^* \rho \omega k + \frac{\partial}{\partial x_j}\left[(\mu + \sigma_k \mu_t)\frac{\partial k}{\partial x_j}\right] \tag{1}$$

$$\frac{\partial(\rho \omega)}{\partial t} + \frac{\partial(\rho u_j \omega)}{\partial x_j} = \frac{\alpha \omega}{k} P_k - \beta \rho \omega^2 + \frac{\partial}{\partial x_j}\left[(\mu + \sigma_\omega \mu_t)\frac{\partial \omega}{\partial x_j}\right] + 2(1 - F_1)\frac{\rho \sigma_{\omega 2}}{\omega}\frac{\partial k}{\partial x_j}\frac{\partial \omega}{\partial x_j} \tag{2}$$

where the production term $P_k$ can be expressed by:

$$P_k = \tau_{ij}\frac{\partial u_i}{\partial x_j} \tag{3}$$

$$\tau_{ij} = \mu_t\left(2S_{ij} - \frac{2}{3}\frac{\partial u_k}{\partial x_k}\delta_{ij}\right) - \frac{2}{3}\rho k\delta_{ij} \tag{4}$$

where $\delta_{ij}$ is the Kronecker number and $S_{ij}$ is the shear-stress tensor, so that

$$S_{ij} = \frac{1}{2}\left(\frac{\partial u_i}{\partial x_j} + \frac{\partial u_j}{\partial x_i}\right) \tag{5}$$

and

$$\mu_t = \frac{1}{\max(a_1\omega, SF_2)} \tag{6}$$

$F_1$ is the 1st blending function for variants (for example, $\varphi$), by

$$\varphi = F_1\varphi_1 + (1 - F_1)\varphi_2 \tag{7}$$

where $F_1$ follows

$$F_1 = \tanh\left\{\left\{\min\left[\max\left(\frac{\sqrt{k}}{\beta^*\omega d_w}, \frac{500\nu}{d_w^2\omega}\right), \frac{4\rho\sigma_{\omega 2}k}{CD_{k\omega}d_w^2}\right]\right\}^4\right\} \tag{8}$$

where $d_w$ is the distance to the nearest wall, $\nu$ is the kinematic viscosity, and $CD_{k\omega}$ is

$$CD_{k\omega} = \max\left(2\rho\sigma_{\omega 2}\frac{1}{\omega}\frac{\partial k}{\partial x_j}\frac{\partial \omega}{\partial x_j}, 10^{-20}\right) \tag{9}$$

$F_2$ is the 2nd blending function:

$$F_2 = \tanh\left\{\left[\max\left(2\frac{\sqrt{k}}{\beta^*\omega d}, \frac{500\nu}{d_w^2\omega}\right)\right]^2\right\} \tag{10}$$

In the above equations, $\rho$ is the density. $x$, $t$, and $u$ denote coordinate, time and velocity, respectively. The constants are $\sigma_{k1} = 0.85$, $\sigma_{\omega 1} = 0.65$, $\beta_1 = 0.075$ for the $k$-$\omega$ setup and $\sigma_{k2} = 1.00$, $\sigma_{\omega 2} = 0.856$, $\beta_2 = 0.0828$ for the $k$-$\varepsilon$ setup. The other constants are $\beta^* = 0.09$, $a_1 = 0.31$ and $\alpha = 0.556$.

### 2.2. Wall Treatments

#### 2.2.1. No-Slip Wall

The no-slip wall boundary has been popularly used in computational-fluid-dynamics (CFD) research [22]. It assumes that fluid molecules may not slip from a wall in an ideal situation [28,29]. Generally, a common approximation for fluid slip can be drawn as:

$$u - u_w = \beta_s\frac{\partial u}{\partial n} \tag{11}$$

where $u$ is the fluid velocity, $u_w$ is the velocity on the wall, $\beta_s$ is the slip length so that $\beta_s = C_s \cdot l_{mfp}$ where $l_{mfp}$ is the mean free path and $C_s$ is the empirical coefficient [30]. For a no-slip wall-boundary condition, $\beta_s$ is 0, which means $u = u_w$.

### 2.2.2. Automatic-Wall Functions

If the SST turbulence model was applied, the automatic-wall treatments [6] were also adopted, to empirically model the near-wall flow. As shown in Figure 1, the red line in the figure is the change curve of fluid velocity with the distance from the wall. The near-wall-flow region included 3 main parts: the viscous sublayer, buffer layer and logarithmic layer [31,32]. In the viscous sublayer, there is [33]:

$$u^+ = y^+ \tag{12}$$

where $u^+$ is the dimensionless velocity of t $u^+ = u/u_t$; $u$ is the velocity, $u_t$ is the friction velocity of $u_t = \sqrt{\tau_w/\rho}$., $\tau_w$ is the wall shear stress, and $y^+$ is the dimensionless off-wall distance of $y^+ = y{\cdot}u_t$, where $y$ is the off-wall distance. In the logarithmic layer, there is [33]:

$$u^+ = \frac{1}{\kappa}\ln y^+ + C^+ \tag{13}$$

where $\kappa$ is the von Karman constant and $C^+$ is the velocity-deviation constant. The automatic-wall functions blend the $\omega$ solution and the $u_t$ solution by [34]

$$\omega = \sqrt{\omega_{vis}^2 + \omega_{log}^2} \tag{14}$$

$$u_t = \sqrt[4]{\left(u_t^{vis}\right)^4 + \left(u_t^{log}\right)^4} \tag{15}$$

where superscript/subscript *vis* represent the viscous sublayer and the buffer layer, respectively, and superscript/subscript *log* represent the logarithmic layer.

$$\omega_{vis} = \frac{6\nu}{\beta y^2}; \omega_{\log} = \frac{u_t}{C_\mu^{1/4}\kappa y} \tag{16}$$

$$u_t^{vis} = \frac{u}{y^+}; u_t^{log} = \frac{u}{\log E_u y^+} \tag{17}$$

where $E_u$ is the model constant of 9.81, and $C_\mu$ is the eddy-viscosity coefficient. Here we define $y$ as the mesh-element–centroid off-wall distance in the CFD simulation; if the $y$ value is small, $1/y^2$ dominates, to emphasize the viscous characters. On the contrary, if the $y$ value is large, $1/y$ dominates, being mainly logarithmic.

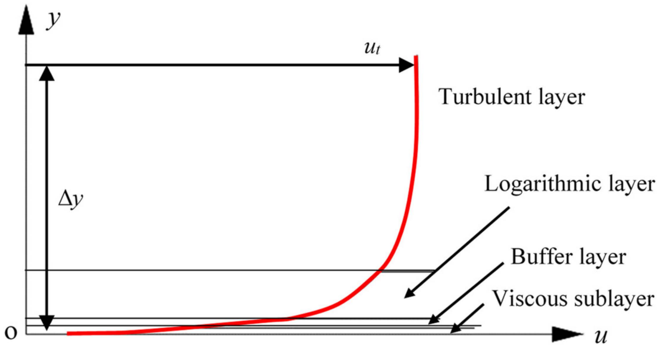

**Figure 1.** Law of the near-wall velocity distribution. u: velocity; y: off-wall distance.

### 2.2.3. Immersed-Solid Method

The immersed-solid method is enabled in the commercial software ANSYS CFX by immersing a rigid-solid domain into a fluid domain [14]. This immersed-solid domain was more like a region in which a momentum source is added to force the fluid to move with the solid. Figure 2 shows a schematic map of the mesh elements and nodes when using the immersed-solid method. Table 1 lists the acronyms defined for the immersed-solid method.

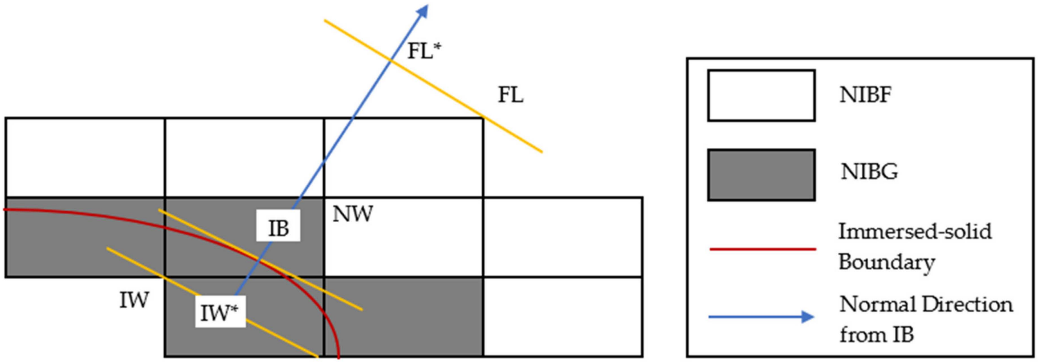

**Figure 2.** Schematic map of the mesh elements and nodes when using the immersed-solid method.

**Table 1.** The acronyms defined for the immersed-solid method.

| Acronyms | Meaning |
|---|---|
| IW | In-wall node |
| IW* | In-wall point |
| NW | Near-wall node |
| IB | Point on the immersed-solid boundary |
| FL | Fluid node |
| FL* | Fluid point |
| NIBG | Elements between NW and IW nodes |
| NIBF | Elements between NW and FL nodes |

In ANSYS CFX, there are some important settings for the immersed-solid method, as follows:

- Wall distance: 0 on the nodes inside the immersed solid; a function of the wall scales on the nodes near the inside of the immersed solid; the physical distance of the nodes near the immersed solid was achieved using the boundary-tracking method for wall functions.
- $k$ and $\omega$ in SST turbulence-model cases: 0 on the nodes inside the immersed solid; scalable-wall treatment was used for $\omega$ in the logarithmic region by $\omega_{log} = u^{*2}/(C_{\mu}{}^{1/2}\kappa\nu y^{*})$ where $u^{*} = C_{\mu}{}^{1/2}k^{1/4}$ and $y^{*} = u^{*}\Delta y/\nu$. The value of $\Delta y$ is the distance between the node near the immersed solid and the immersed-solid boundary. The $y$* value is lowered to 11.06 for dividing the logarithmic region and the linear viscous region.
- Friction velocity $u_t$: Based on the scalable-wall treatment, $u_t$ in the logarithmic region is $u_t{}^{log} = \Delta U/[1/\kappa\ln(y^{*}) + C] = \Delta U/u^{+}$, where $\Delta U$ is the fluid tangential velocity relative to the immersed boundary.

According to the setup above, the velocity on the near-wall nodes can be forced as

$$\left(U_{NW}^{F}\right)_{tan} = \left(U_{IB}^{IS}\right)_{tan} + \frac{(u^{*}/u^{+})_{FL}}{(u^{*}/u^{+})_{NW}}\left[(U_{FL})_{tan} - \left(U_{IB}^{IS}\right)_{tan}\right] \tag{18}$$

where superscript $F$ and $IS$ denote the fluid and immersed solid, respectively. The momentum source can be calculated based on the tangential-force velocity $(U_{NW}{}^{F})_{tan}$ and the wall-normal velocity $(U_{IB}{}^{IS})_{nm}$:

$$U_{NW}^{F} = \left(U_{NW}^{F}\right)_{tan} + \left(U_{IB}^{IS}\right)_{nm} \tag{19}$$

Hence, fluid can be prevented from getting through the immersed-solid domain.

## 3. Studied Object

### 3.1. NACA0015 Profile

The NACA0015 [35] profile belongs to the typical NACA four-digit-profile series. It is symmetric along the meanline. If we define the foil-meanline direction as $m_f$ and the thickness direction (the origin from the meanline) as $t_f$, the NACA0015 $m_f$ -$t_f$ profile can be illustrated in Figure 3, where the total length along $m_f$ is denoted as $c$ and the maximum thickness is denoted as $t_{fm}$. The relationship between $t_f$ and $m_f$ can be expressed as:

$$\pm\frac{t_f}{c}=\frac{t_{mf}}{0.2c}\left[0.297\sqrt{\frac{m_f}{c}}-0.126\left(\frac{m_f}{c}\right)-0.352\left(\frac{m_f}{c}\right)^2+0.284\left(\frac{m_f}{c}\right)^3-0.102\left(\frac{m_f}{c}\right)^4\right] \quad (20)$$

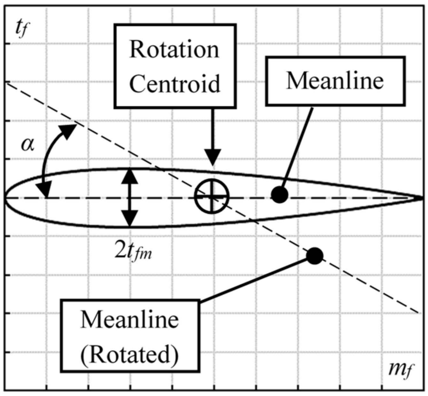

**Figure 3.** The NACA0015 hydrofoil profile.

In addition, the leading edge of the NACA0015 profile is an arc, whose radius is $r_{LE}$, as in the following:

$$\frac{r_{LE}}{c}=1.102\left(\frac{t_{mf}}{c}\right)^2 \quad (21)$$

Thus, the maximum thickness, $t_{fm}$, approximately locates at $m_f/c$ = 0.3. The incidence angle (between the meanline and rotated meanline) can be denoted as $\alpha$, the unit representing a degree. It represents the foil-rotation status, based on the rotation centroid.

### 3.2. Case Detail

In this study, the NACA0015 foil was studied at $\alpha$ = 8 degrees inside an $L_1 \times L_2 \times L_3$ cuboid domain, as shown in Figure 4. $L_1$, $L_2$ and $L_3$ were respectively equal to 4.35$c$, 1.04$c$ and 0.70$c$. Coordinate components $X$, $Y$ and $Z$ denote the three orthogonal directions, where $X$ is along the flow direction, $Y$ is perpendicular to the flow direction and $Z$ is along the foil span. Because the foil does not change shape and scale along $Z$, this 3D case can be treated as an $X$-$Y$ quasi-2D case, which provides a good case simplification. Fluid flows into the domain at the inlet boundary and out of the domain at the outlet boundary. The four surrounding $X$-$Y$ and $X$-$Z$ planes are walls.

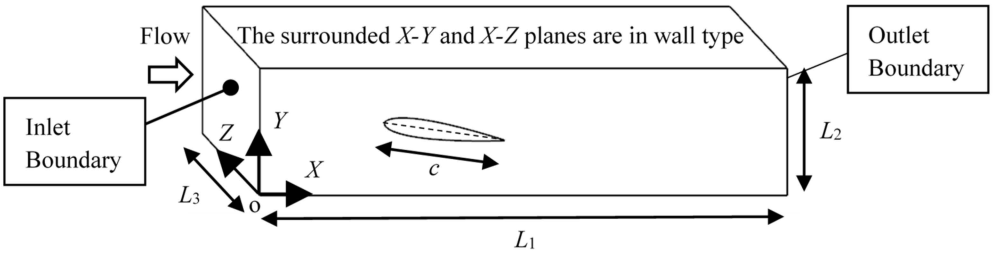

**Figure 4.** The 3D-flow domain with NACA0015 foil at incidence angle of 8 degrees.

### 3.3. Computational-Fluid-Dynamics Setups

In this case, the hydrodynamic characters were mainly studied. ANSYS CFX was used as the CFD solver by using the unsteady-RANS method with the SST turbulence model, as introduced in the above sections. The fluid medium was set as water at 20 °C under the 1 atm pressure environment. Compressibility, heat transfer and mass transfer were not considered. The advection scheme and the turbulence numeric were set as high resolution. The inlet boundary was set as velocity inlet with uniform $V_{in}$ distribution, and the pressure at the inlet was at zero gradient. The outlet boundary was set as the static-pressure boundary of relatively 0 Pa, and the velocity at the outlet was at zero gradient. The surrounded walls were set as no-slip type. The foil surface was compared, between the no-slip type and the immersed-solid type. In this case, the Reynolds number, $Re$, was $5.0 \times 10^5$, according to the following equation:

$$Re = \frac{\rho c V_{in}}{\mu} \tag{22}$$

The unsteady simulation was based on the steady simulation of 600 iterations. The unsteady simulation covered a total of 0.1 s and spent 0.0001 s on each time step. The maximum iteration number for each time step was 10, with the convergence criteria of RMS $1.0 \times 10^{-5}$.

## 4. Numerical-Accuracy Check and Validation

### 4.1. No-Slip Wall Case

In the no-slip-wall case (the foil surface was set as the no-slip wall), the domain was meshed by structural hexahedral elements, using ICEMCFD. Six different mesh schemes, whose node number increased proportionally and gradually, as listed in Table 2, were comparatively checked for accuracy by comparing the numerically predicted pressure with the experimentally tested pressure [15] on the foil surface along the $X$ direction. In this case, the dimensionless pressure coefficient, $C_p$, was used:

$$C_p = \frac{p - p_{in}}{0.5\rho V_{in}^2} \tag{23}$$

where $p$ is the pressure, and $p_{in}$ is the pressure at the inlet boundary. The position along the $X$ direction is also in a relative form, as $X/c$.

**Table 2.** Mesh schemes checked in the no-slip-wall case.

| No. | Node Number | Description |
|---|---|---|
| 1 | 30,884 | Very Coarse |
| 2 | 62,496 | Coarse |
| 3 | 107,652 | Mid-Coarse |
| 4 | 175,150 | Mid-Fine |
| 5 | 257,488 | Fine |
| 6 | 352,594 | Very Fine |

Figure 5 shows the pressure on the foil surface under different mesh schemes by treating the foil surface as no-slip wall boundary. In addition, the near-wall region where $y^+$ was 1.45~16.22 was predicted by automatic-wall functions. The Nos. one to six mesh schemes predicted the pressure well from $X/c \approx 0.4$ to $X/c \approx 1.0$ by comparing it with the experimental data [15]. However, the main difference occurred in the front 20% $X/c$ region, especially on the foil-suction side. The minimum $C_p$ value for the coarse mesh was larger than $-3$. Then, it decreased to $-3$~$-3.25$ in the simulations for coarse, mid-coarse and mid-fine meshes. When the mesh nodes increased to 257488 (fine), the numerically predicted $C_p$ curve overlapped well with the experimental data. This situation occurred when the mesh nodes increased to 352594 (very fine). Usually, we called this "mesh independence". Thus, the mesh scheme No. five with 257488 modes can be selected in this study, with good accuracy.

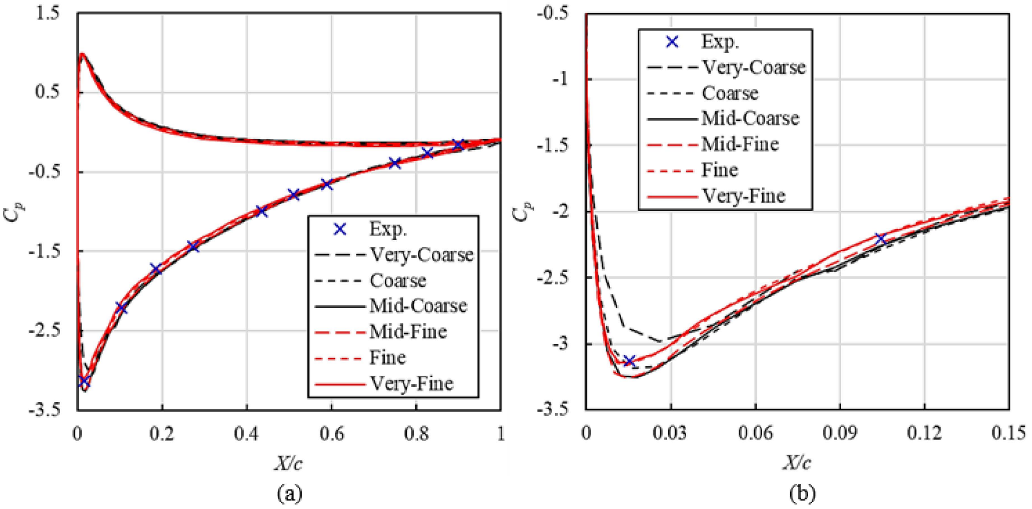

**Figure 5.** Pressure on foil surface under different mesh schemes. (**a**) $C_p$ distribution on foil surface along $X$ direction; (**b**) Enlarged view within $X/c$ = 0~0.15 and $C_p$ = $-0.5$~$-3.5$.

## *4.2. Immersed-Solid Case*

The foil surface was also treated as the immersed-solid boundary. In this situation, four different mesh combinations were discussed, as listed in Table 3. The pressure distribution on the foil surface was also analyzed along the $X$ direction. The dimensionless $C_p$ and relative $X/c$ were still used, as shown in Figure 6.

**Table 3.** Mesh combinations checked in the immersed-solid case.

| No. | Node Number | | | Description |
|---|---|---|---|---|
| | Fluid | Solid | Total | |
| 1 | 234,248 | 51,720 | 291,368 | Coarse |
| 2 | 753,984 | 378,840 | 1,132,824 | Fine |
| 3 | 234,248 | 51,720 | 291,368 | Coarse with Boundary Tracking (Coarse-B) |
| 4 | 753,984 | 378,840 | 1,132,824 | Fine with Boundary Tracking (Fine-B) |

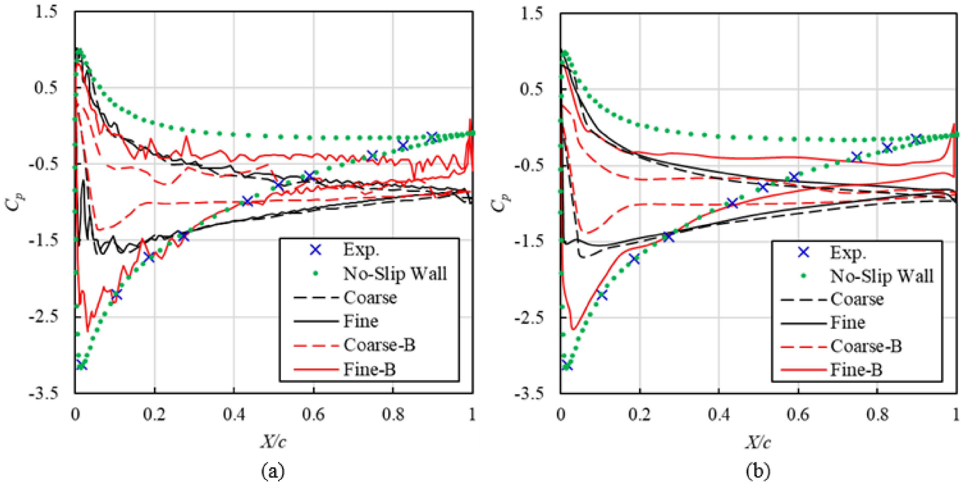

**Figure 6.** Pressure on foil surface under different mesh-scheme combinations. (**a**) $C_p$ distribution on foil surface along $X$ direction; (**b**) Smoothed $C_p$ curves.

Figure 6a shows the pressure on the foil surface under different mesh-scheme combinations. The pulsations can be observed on the immersed-solid predicted $C_p$ curves. These pulsations could be caused by the data interpolation on the fluid–solid interface. Thus, the smooth procedures [36] were conducted to create Figure 6b. The No. 1 combination had the same density as the selected No. 5 mesh in the no-slip-wall case. However, it produced a completely wrong $C_p$ curve, compared with the no-slip-wall case and the experimental data. Therefore, the mesh density was refined to No. 2, but no improvement could be observed. Based on the two results, the boundary tracking was set to near-wall approximations on the immersed solid on the fluid side. The "Coarse-B" curve still produced wrong data. On the other hand, the "Fine-B" curve showed an obvious improvement, in that both the leading-edge pressure rise and drop were correctly captured in position. The amplitude of the maximum and minimum $C_p$ values became closer to the experimental data. Therefore, the other flow characteristics will be analyzed in the next section.

## 5. Comparative-Flow Analysis

### 5.1. Forces and Torques

The lift force, $F_Y$, (along the Y direction) and the drag force, $F_X$, (along the X direction) are analyzed in Table 4. In the no-slip-wall case, the lift force was 113.01 N, which was larger than that in the immersed-solid case, of 90.82 N. The drag force was 4.95 N in the no-slip-wall case, which was smaller than that in the immersed-solid case, of 8.67 N. As a result, the immersed-solid method obtained a smaller lift/drag ratio compared with the no-slip-wall setup, with its lift/drag ratio being approximately 40% of the no-slip-wall case. The torques on the foil on the base of the rotation centroid, $T_Z$, were also predicted, as is also shown in Table 4. In the no-slip-wall case, the foil torque was 3.29 N·m. In the immersed-solid case, the foil torque was 2.31 N·m, which was approximately 70% of the no-slip-wall case. Under the two wall conditions, the difference between the force and torque obtained by numerical simulation is very obvious. In order to understand the reasons for the differences, we need to analyze the internal flow under different circumstances.

**Table 4.** Lift force, drag force and torque on hydrofoil.

| | **No-Slip-Wall Case** | **Immersed-Solid Case** |
|---|---|---|
| Lift Force, $F_Y$ | 113.01 [N] | 90.82 [N] |
| Drag Force, $F_X$ | 4.95 [N] | 10.48 [N] |
| Lift/Drag Ratio, $F_Y/F_X$ | 22.83 | 8.67 |
| Torque, $T_Z$ | 3.29 [N·m] | 2.31 [N·m] |

### 5.2. Pressure-Coefficient $C_p$ Field

Figure 7 compares the $C_p$ contour on the $X$-$Y$ plane at middle $Z$ position in the domain. The contours in the no-slip case and immersed-solid case were similar. Generally, the flow striking on the foil leading edge was correctly captured in both the two cases. The flow separation after the leading edge was also simulated. Therefore, the immersion-solid method can better simulate the pressure distribution in the flow. However, some differences can be found. Firstly, the very low $C_p$ region ($C_p < -2.5$) on the foil upper side was wider in the no-slip-wall case than in the immersed-solid case. Secondly, $C_p$ increased rapidly in the upper flow field in the no-slip-wall case. However, the $C_p$ increase was relatively slow in the immersed-solid case. Thirdly, there was a high-pressure region in the lower flow field in the no-slip wall case. In the immersed-solid case, the pressure there was relatively low. In the case of the no-slip wall, the pressure difference between the upper and lower sides of the foil was large, which resulted in the lift of the foil being greater than in the case of the immersed solid. Fourthly, in the no-slip-wall case, except for the very low $C_p$ region, the pressure coefficient in other regions was higher than that in the immersed-solid case.

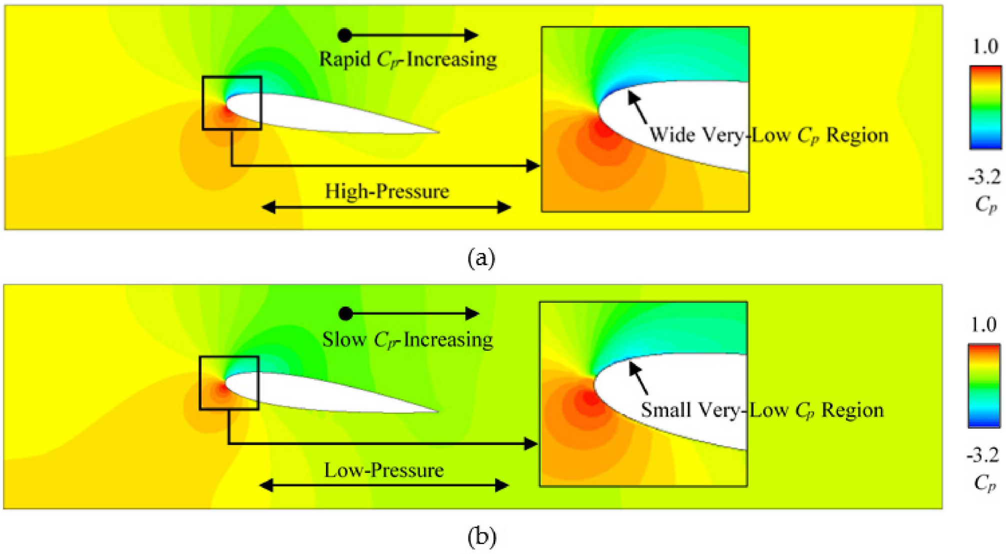

**Figure 7.** The $C_p$ contour on the $X$–$Y$ plane at middle $Z$ position. (**a**) No-slip wall case; (**b**) Immersed-solid case.

### 5.3. Velocity-Coefficient $C_v$ Field

Figure 8 compares the velocity field on the $X$-$Y$ plane at middle $Z$ position in the domain. The velocity was relative to the domain-inlet velocity as a velocity coefficient $C_v = V/V_{in}$. The contours in the no-slip case and immersed-solid case were qualitatively similar but quantitatively different. The leading-edge high-velocity region was captured in the two cases. However, the very high $C_v$ region ($C_v > 1.5$) was wide in the no-slip-wall case but small in the immersed-solid case, and its distribution was basically consistent with the distribution of the very low $C_p$ region. The low velocity after the trailing edge (the wake) was narrow in the no-slip-wall case, but very wide in the immersed-solid case. A high $C_v$ region was in the lower flow field, as indicated in Figure 8b. This shows that the immersed-method underestimates the flow velocity at the leading and trailing edges of the foil, and overestimates the flow velocity of the upper and lower flow fields of the foil.

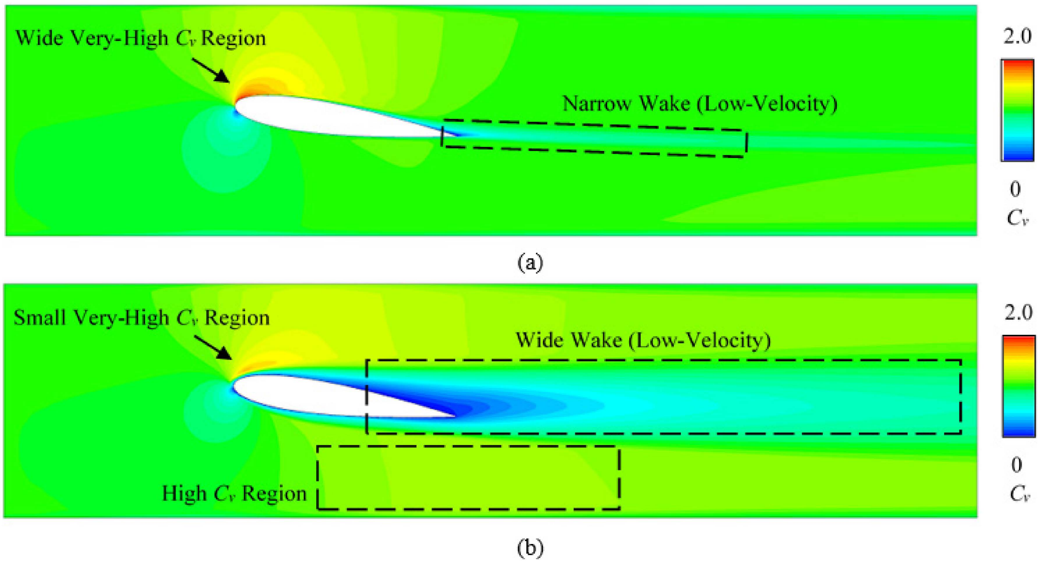

**Figure 8.** The $C_v$ contour on the $X$–$Y$ plane at middle $Z$ position. (**a**) No-slip-wall case; (**b**) Immersed-solid case.

### 5.4. *Turbulence-Kinetic-Energy, k, Field*

Figure 9 shows the turbulence kinetic-energy, $k$, contour on the $X$-$Y$ plane at middle $Z$ position. The legend ranged from 0 to 3.9 $m^2/s^2$. It can be seen from the figure that the turbulence-kinetic-energy, $k$, contours in the two cases are quite different. In the no-slip-wall case, there is a relatively high $k$ region from the foil trailing edge to downstream. It was narrow and relatively weaker than in the immersed-solid case. On the contrary, in the immersed-solid case, the high $k$ region was very wide, covering the entire foil and extending to the downstream far field. The highest $k$ (up to 3.7~3.9) occurred at two main locations, the upper surface near the leading edge and the lower surface, near the trailing edge. Compared with the no-slip-wall case, in the immersed-solid case, the turbulent-kinetic energy of the fluid was higher, resulting in a greater flow loss of the fluid and greater drag coefficient on the foil.

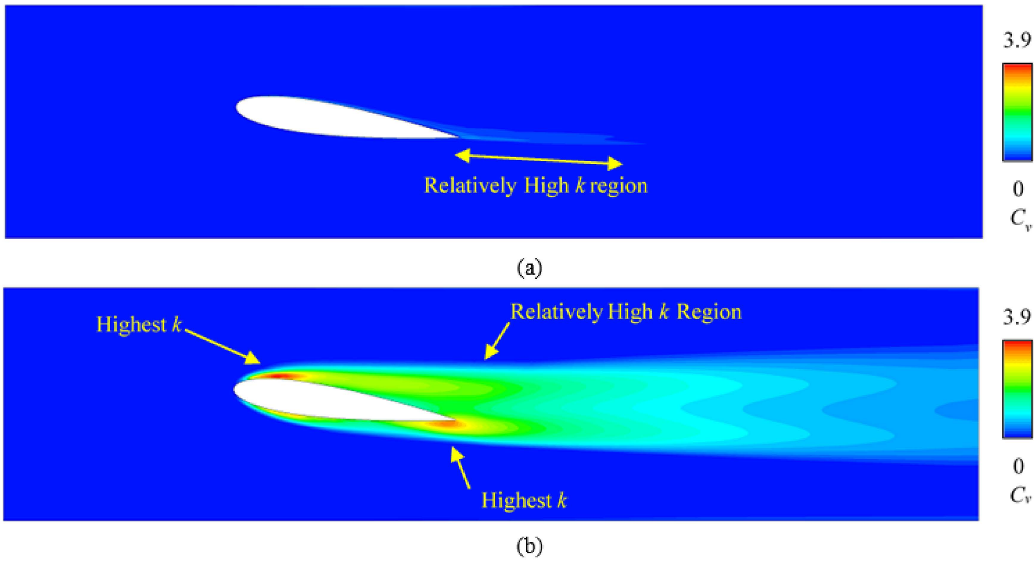

(a)

(b)

**Figure 9.** The $k$ contour on the $X$–$Y$ plane at middle $Z$ position. (**a**) No-slip-wall case; (**b**) Immersed-solid case. Unit of $k$: $[m^2/s^2]$.

## 6. Convergence-Ability Analysis

The convergence ability was analyzed based on the No. 5 mesh scheme in the no-slip-wall case and the No. 4 mesh combination in the immersed-solid case. The two computations were conducted on the same terminal, using 48-core 2.60 GHz CPU and 32.0 GB memory. The solver settings were also the same for the two cases. Table 5 compares the total mesh nodes, element number and timestep number. When the cases were converged to RMS $1.0 \times 10^{-5}$, the clock time until convergence, the clock time per timestep and the clock time per mesh node were also compared.

**Table 5.** Convergence Ability Based on the Steady-State Simulation.

| | **No-Slip-Wall Case** | **Immersed-Solid Case** |
|---|---|---|
| Total Mesh-Node Number, $N_{mn}$ | 257,488 | 1,132,824 |
| Total Mesh-Element Number | 241,542 | 1,077,732 |
| Timesteps Converged to RMS, $1.0 \times 10^{-5}$ $S_{cc}$ | 236 | 81 |
| Clock Time until Convergence, $t_{cc}$ | 1782.6 [s] | 1440.3 [s] |
| Clock Time per Timestep, $t_{cc}/S_{cc}$ | 7.55 [s] | 17.78 [s] |
| Clock Time per Mesh Node, $t_{cc}/M_{mn}$ | 0.0069 [s] | 0.0013 [s] |

According to the mesh check in Section 4, the immersed-solid method needed more mesh nodes than using the no-slip wall to obtain equal accuracy. However, the clock time per mesh node in the immersed-solid case was shorter than that in the no-slip-wall case. The immersed-solid case needed a lower timestep number to be converged than the no-slip-wall case. However, the clock time per timestep was longer in the immersed-solid case than that in the no-slip-wall case. Generally, the immersed-solid case converged to RMS $1.0 \times 10^{-5}$ in 1440.3 s, which was shorter than the 1782.6 s in the no-slip-wall case. The time consumption of the immersed-solid setup in this study took 80.7% of the clock time of the traditional no-slip-wall setup. Because the memory consumption was proportional to the mesh number, the immersed-solid setup in this study consumed 4.39 times the memory of the traditional no-slip-wall setup.

## 7. Conclusions

As an available option in the commercial software ANSYS CFX, the immersed-solid method can flexibly add wall boundaries in the fluid domain. In this study, under the typical hydrodynamic condition of the flow around the hydrofoil, without considering the hydrofoil movement, the immersed-solid method is compared with the non-slip-wall boundary, and the effectiveness of the immersed-solid method to simulate extremely small leakage, changing leakage, and randomly moving/rotating solid and intermittent attaching/detaching solids is verified, and the following conclusions are drawn. (A) The results of the immersed-solid method were qualitatively correct but quantitatively inaccurate. (B) "Boundary tracking" was crucial for improving the near-wall solution. (C) More mesh nodes were required for the qualitatively correct result when using the immersed-solid method than when using the no-slip wall. (D) The curve-smoothing process was recommended to correct the "pulsation" around the fluid–solid interface, due to data interpolation.

In detail, the flow-striking and separation positions on the solid can be correctly captured by both the no-slip-wall and immersed-solid method. However, the pressure fields and velocity fields performed differently, especially at the downstream location. A much wider wake could be found using the immersed-solid method than in the no-slip-wall case. Because of the added momentum source, the immersed-solid method prevented fluid passing through the hydrofoil. At this time, high turbulence-kinetic energy was triggered around the foil surface, especially at the flow-striking, separation and wake positions.

Generally, the immersed-solid method can accurately simulate the flow field by setting reasonable mesh nodes, especially on the fluid–solid interface. The convergence ability of the immersed-solid method is better than the no-slip-wall setup. If we apply the immersed-solid method to special cases such as extremely small leakage, changing leakage, randomly moving/rotating solid and intermittent attaching/detaching solids, it will provide us with a fast hydrodynamic solution, by overcoming the problems caused by excessive mesh density, mesh deformation or domain change. The research results of this paper have great engineering value, especially in the engineering-flow cases.

**Author Contributions:** Conceptualization, R.X. and R.T.; writing—original draft preparation, Z.H. and D.Z.; writing—review and editing, R.X. and D.Z.; supervision, R.T. and D.Z. All authors have read and agreed to the published version of the manuscript.

**Funding:** This research is supported by the Open Research Subject of Key Laboratory of Fluid and Power Machinery (Xihua University), Ministry of Education (grant number LTDL-2022009).

**Institutional Review Board Statement:** Not applicable.

**Informed Consent Statement:** Not applicable.

**Data Availability Statement:** Data available on request from the corresponding author.

**Acknowledgments:** The authors would like to acknowledge the help from Zhengwei Wang and his research group at Tsinghua University.

**Conflicts of Interest:** The authors declare no conflict of interest.

## References

1. Kan, K.; Zhang, Q.; Zheng, Y.; Xu, H.; Xu, Z.; Zhai, J.; Muhirwa, A. Investigation into Influence of Wall Roughness on the Hydraulic Characteristics of an Axial Flow Pump as Turbine. *Sustainability* **2022**, *14*, 8459. [CrossRef]
2. Tong, Z.; Xin, J.; Ling, C. Many-Objective Hybrid Optimization Method for Impeller Profile Design of Low Specific Speed Centrifugal Pump in District Energy Systems. *Sustainability* **2021**, *13*, 10537. [CrossRef]
3. Wendt, J.F.; Anderson, J.D. Basic Philosophy of CFD. In *Computational Fluid Dynamics: An Introduction*; Spinger: Berlin/Heidelberg, Germany, 2009; pp. 5–8.
4. Kajishima, T.; Taira, K. Numerical Simulation of Fluid Flows. In *Computational Fluid Dynamics*; Springer: Berlin/Heidelberg, Germany, 2017; pp. 1–22.
5. Grotjans, H.; Menter, F.R. Wall Functions for General Application CFD Codes. *Comput. Fluid Dyn.* **1998**, *1*, 1112–1117.
6. Kader, B.A. Temperature and Concentration Profiles in Fully Turbulent Boundary Layers. *Int. J. Heat Mass Transf.* **1981**, *24*, 1541–1544. [CrossRef]
7. Patel, V.C.; Rodi, W.; Scheuerer, G. Turbulence Models for Near-Wall and Low Reynolds Number Flows—A Review. *AIAA J.* **1985**, *23*, 1308–1319. [CrossRef]
8. Ha, T.W.; Choe, B.S. Numerical Simulation of Rotordynamic Coefficients for Eccentric Annular-Type-Plain-Pump Seal Using CFD Analysis. *J. Mech. Sci. Technol.* **2012**, *26*, 1043–1048. [CrossRef]
9. Blanco, A.M.; Oro, J.F. Unsteady Numerical Simulation of an Air-Operated Piston Pump for Lubricating Greases Using Dynamic Meshes. *Comput. Fluids* **2012**, *57*, 138–150. [CrossRef]
10. Akoz, M.S.; Kirkgoz, M.S.; Oner, A.A. Experimental and Numerical Modeling of a Sluice Gate Flow. *J. Hydraul. Res.* **2009**, *47*, 167–176. [CrossRef]
11. Qun-feng, Z.; Pan-pan, Y.A.N.; Jian-ping, S.; Wan-fa, H.E. Numerical Simulation of Inlet and Outlet Pressures Influencing Internal Flow of a Vane Pump. *Acta Armamentarii* **2014**, *35*, 1223.
12. Adkins, D.; Yan, Y.Y. CFD Simulation of Fish-like Body Moving in Viscous Liquid. *J. Bionic. Eng.* **2006**, *3*, 147–153. [CrossRef]
13. Jin, C.; Xu, K.; Chen, S. A Three Dimensional Gas-Kinetic Scheme with Moving Mesh for Low-Speed Viscous Flow Computations. *Adv. Appl. Math. Mech* **2010**, *2*, 746–762. [CrossRef]
14. Kajishima, T.; Takeuchi, S. Simulation of Fluid-Structure Interaction Based on an Immersed-Solid Method. *J. Mech. Eng. Sci.* **2013**, *5*, 555–561. [CrossRef]
15. Yoon, Y.; Park, B.-H.; Shim, J.; Han, Y.-O.; Hong, B.-J.; Yun, S.-H. Numerical Simulation of Three-Dimensional External Gear Pump Using Immersed Solid Method. *Appl. Therm. Eng.* **2017**, *118*, 539–550. [CrossRef]
16. Zhang, W.; Jiang, Q.; Bois, G.; Li, H.; Liu, X.; Yuan, S.; Heng, Y. Experimental and Numerical Analysis on Flow Characteristics in a Double Helix Screw Pump. *Energies* **2019**, *12*, 3420. [CrossRef]
17. Qiu, R.; Zhang, W.; Jiang, Q.; Shen, K.; Gread, B.; Yuan, S. Research on Full Flow Passage Characteristics of Double Screw Pump Based on Immersion Entity Method. In *Proceedings of the Journal of Physics: Conference Series*; IOP Publishing: Bristol, UK, 2022; Volume 2186, p. 012015.
18. Cervone, A.; Bramanti, C.; Rapposelli, E.; d'Agostino, L. Thermal Cavitation Experiments on a NACA 0015 Hydrofoil. *J. Fluids Eng.* **2006**, *128*, 326–331. [CrossRef]
19. Dreyer, M.; Decaix, J.; Münch-Alligné, C.; Farhat, M. Mind the Gap: A New Insight into the Tip Leakage Vortex Using Stereo-PIV. *Exp. Fluids* **2014**, *55*, 1849. [CrossRef]
20. Nowruzi, H.; Ghassemi, H.; Ghiasi, M. Performance Predicting of 2D and 3D Submerged Hydrofoils Using CFD and ANNs. *J. Mar. Sci. Technol.* **2017**, *22*, 710–733. [CrossRef]
21. Hu, C.; Chen, G.; Yang, L.; Wang, G. Large Eddy Simulation of Turbulent Attached Cavitating Flows around Different Twisted Hydrofoils. *Energies* **2018**, *11*, 2768. [CrossRef]
22. Day, M.A. The No-Slip Condition of Fluid Dynamics. *Erkenntnis* **1990**, *33*, 285–296. [CrossRef]
23. Schmitt, F.G. About Boussinesq's Turbulent Viscosity Hypothesis: Historical Remarks and a Direct Evaluation of Its Validity. *Comptes Rendus Mécanique* **2007**, *335*, 617–627. [CrossRef]
24. Menter, F.R.; Kuntz, M.; Langtry, R. Ten Years of Industrial Experience with the SST Turbulence Model. *Turbul. Heat Mass Transf.* **2003**, *4*, 625–632.
25. Launder, B.E.; Spalding, D.B. The Numerical Computation of Turbulent Flows. In *Numerical Prediction of Flow, Heat Transfer, Turbulence and Combustion*; Elsevier: Amsterdam, The Netherlands, 1983; pp. 96–116.
26. Wilcox, D.C. Formulation of the K-w Turbulence Model Revisited. *AIAA J.* **2008**, *46*, 2823–2838. [CrossRef]
27. Menter, F.R. Two-Equation Eddy-Viscosity Turbulence Models for Engineering Applications. *AIAA J.* **1994**, *32*, 1598–1605. [CrossRef]
28. Shu, J.-J.; Bin Melvin Teo, J.; Kong Chan, W. Fluid Velocity Slip and Temperature Jump at a Solid Surface. *Appl. Mech. Rev.* **2017**, *69*, 020801. [CrossRef]
29. Shu, J.-J.; Teo, J.B.M.; Chan, W.K. A New Model for Fluid Velocity Slip on a Solid Surface. *Soft Matter* **2016**, *12*, 8388–8397. [CrossRef]
30. Morris, D.L.; Hannon, L.; Garcia, A.L. Slip Length in a Dilute Gas. *Phys. Rev. A* **1992**, *46*, 5279–5281. [CrossRef]
31. Pope, S.B. The Scales of Turbulent Motion. *Turbul. Flows* **2000**, *1*, 195–197.

32. Pöschl, T. Mechanische Ähnlichkeit. In *Lehrbuch der Technischen Mechanik für Ingenieure und Physiker*; Springer: Berlin/Heidelberg, Germany, 1930; pp. 307–311.
33. Yang, X.I.A.; Xia, Z.-H.; Lee, J.; Lv, Y.; Yuan, J. Mean Flow Scaling in a Spanwise Rotating Channel. *Phys. Rev. Fluids* **2020**, *5*, 074603. [CrossRef]
34. Menter, F.; Esch, T. Elements of Industrial Heat Transfer Predictions. In Proceedings of the 16th Brazilian Congress of Mechanical Engineering (COBEM), Uberlândia, Brazil, 26–30 November 2001; Volume 109, p. 650.
35. Abbott, I.H.; Von Doenhoff, A.E. *Theory of Wing Sections*; Dover Publications: Mineola, NY, USA, 1959; pp. 112–115.
36. Arlinghaus, S. *Practical Handbook of Curve Fitting*; CRC Press: Boca Raton, FL, USA, 1994; ISBN 0-8493-0143-2.